Heliyon 10 (2024) e34517

Contents lists available at ScienceDirect

Heliyon

journal homepage: www.cell.com/heliyon

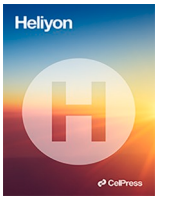

Research article

Photodegradation, kinetics and non-linear error functions of methylene blue dye using $SrZrO_3$ perovskite photocatalyst

J.N. Tsaviv [a,**], I.S. Eneji [a,***], R. Sha'Ato [a], I. Ahemen [b], P.R. Jubu [b,*], Y. Yusof [c]

[a] Department of Chemistry, Joseph Sarwuan Tarka University, P.M.B. 2373, Makurdi, Benue State, Nigeria
[b] Department of Physics, Joseph Sarwuan Tarka University, P.M.B. 2373, Makurdi, Benue State, Nigeria
[c] Nano-optoelectronic Research Laboratory, School of Physics, Universiti Sains Malaysia, 11800, Pinang, Malaysia

ARTICLE INFO

Keywords:
Photocatalysis
Adsorption
Kinetics
Perovskite
Photodegradation

ABSTRACT

The degradation of methylene blue dye-contaminated wastewater via photocatalysis is an efficient approach towards environmental remediation. The $SrZrO_3$ perovskite photocatalyst was synthesized using the modified Pechini sol-gel method, and characterized using XRD, FESEM, FTIR, and UV–visible spectrophotometer. Crystallite size obtained by the Scherrer and Williamson-Hall methods were 45.56 and 44.50 nm, respectively. The sample exhibited an orthorhombic crystal structure. The optical bandgap was estimated to be 5.31 eV. Kinetic study for the degradation of methylene blue dye using $SrZrO_3$ in the presence of H_2O_2 showed complete decontamination of the methylene blue dye in the time interval of 90–120 min under visible light irradiation. The degradation efficiency was above 80.1 % under illumination and less than 40.1 % in dark. Kinetic studies were performed by varying the dose of photocatalyst and initial concentration of methylene blue. It was observed that higher dose of the photocatalyst and lower concentration of the contaminant produced higher rate of degradation. The solution pH 3 and catalysts dosage of 200 mg yielded the highest rate of degradation. The experimental data fitted best into the Psuedosecond order kinetic model with the highest R^2 value, indicating a strong linear relationship. The experimental data was subjected into nonlinear error functions, where the Psuedo-second order kinetic model demonstrated lower values of error functions. The results suggest that the prepared $SrZrO_3$ photocatalyst coupled H_2O_2 is a promising photocatalyst for the decontamination of methylene blue dye under visible light irradiation.

1. Introduction

The sixth millennium development goal stipulates that everyone has the right to sufficient, safe, accessible and affordable clean water for livelihood. However, water quality has been jeopardized due to anthropogenic activities. Water quality becomes unsafe when contaminated [1]. More than 200 different kinds of pharmaceutical and textile effluents have been reported worldwide in freshwater systems [2,3]. Mehdizadeh et al. [4] reported global threat to water on account of organic waste disposal. According to Bryne et al. [5], freshwater contaminants include organic, inorganic and microbial wastes. Water pollution can cause negative effects, such as diseases,

* Corresponding author.
** Corresponding author.
*** Corresponding author.
E-mail addresses: doochivir@gmail.com (J.N. Tsaviv), eneji.ishaqs@uam.edu.ng (I.S. Eneji), peverga.jubu@uam.edu.ng (P.R. Jubu).

https://doi.org/10.1016/j.heliyon.2024.e34517
Received 19 March 2024; Received in revised form 10 July 2024; Accepted 10 July 2024
Available online 11 July 2024

water scarcity and death. Methylene blue dye (MB) effluent is an organic industrial waste from the textile and printing industries that can contaminant freshwater sources, making it unfit for domestic use [6]. The treatment of MB-contaminated wastewater via an efficient process is necessary due to its carcinogenicity and toxicity.

In recent times, perovskite catalysts have received great attention for environmental remediation [7]. They have found applications in chemical sensors, fuel cells, catalyst for energy generation and photocatalyst for wastewater decontamination [8,9]. To be a good photocatalyst, a material must have an acceptable band gap, low charge recombination and photo-corrosion resistance [10]. Photocatalysis is one of the classes of advanced oxidation processes used for decontamination of organic pollutants [11–13]. In this process, photoinduced radical oxygenated species, particularly hydroxyl radicals can oxidize organic pollutants into CO_2 and H_2O [14]. Heterogeneous photocatalysis is one of the advanced oxidation processes used for energy generation and environmental remediation applications [15,16]. Heterogeneous photocatalysts are reported for degradation and removal of dyes, organohalides, petroleum hydrocarbons, heavy metals and pharmaceuticals in soils and liquid effluents [17].

Janaki et al. [18] reported 95 % degradation of MB dye using $LaFeO_3$ supported bentonite via visible light within 60 min irradiation. In a similar study, Yan et al. [19] reported 96.5 % degradation of 5 mg rhodamine under 30 min using $CaTiO_3$-g-C_3N_4 photocatalyst under irradiation with a 200 W Xenon lamp (250 nm $\leq \lambda \leq$ 2500 nm). Zhou et al. [20] reported the fabrication of $LaNiO_3$ nanoparticles modified g-C_3N_4 nanosheets for enhanced visible light driven photocatalysis towards tetracycline degradation. Aravinthkumar et al. [10] synthesized $SrTiO_3$ nanoparticles for enhanced photocatalytic activity and photovoltaic applications. The photodegradation of MB dye under UV illumination yielded an efficiency of 36 %. In a related work, Aravinthkumar et al. [21] incorporated Fe^{3+} ions in $SrTiO_3$ nanosphere for high performances of dye-sensitized solar cell and photocatalytic MB dye degradation, and achieved photodegradation efficiency of 82.57 % under visible light irradiation. Ramakrishnan et al. [22] fabricated TiO_2/CeO_2 core/shell nanostructures for photocatalytic degradation of MB and clitoria ternatea dyes. The workers achieved photodegradation efficiencies of 36 and 71 % for clitoria ternatea and MB dyes under UV light illumination for the period of 40 min. Aravinthkumar et al. [9] reported the photocatalytic degradation efficiency of 88 % for MB dye using Cr doped $SrTiO_3$ interconnected spheres catalyst under visible light illumination. Alvarez-Corena et al. [23] described photocatalysis as a promising wastewater treatment technology for degradation of pharmaceutical contaminants.

$SrZrO_3$ is a wide band gap perovskite material with an orthorhombic structure. It has excellent dielectric, luminescent, catalytic, protonic properties and has been reported for photoelectrochemical water splitting towards H_2 fuel production under UV light [24]. Literature reports are available for the deployment of $SrZrO_3$ for luminescence application [25]. It has been reported that $SrZrO_3$ is promising for photodegradation of MB, since it has been applied for water splitting under UV light [26]. However, $SrZrO_3$ photocatalyst cannot perform optimally under visible light due to its ultra-wide band gap of $\geq$ 5.0 eV that can only absorb light in the UV region of the spectrum. Nevertheless, coupling $SrZrO_3$ with H_2O_2 can mitigate recombination reactions, enable photon absorption in the visible region and enhance photocatalytic activity. Therefore, the present work seeks to extend the literature by employing $SrZrO_3$ coupled with H_2O_2 for degradation of MB under visible light irradiation. The $SrZrO_3$ nanoparticles coupled H_2O_2 was prepared by the modified Pechini method and investigated for the photodegradation of MB at different variables, including dye concentration, solution pH, catalyst dosage and reaction time. Photocatalytic degradation efficiency under visible light was found to be >80 %, indicating that the catalyst has potential for visible light application.

2. Materials and method

2.1. Reagents

All the chemicals used were of analytical grade zirconium-*n*-propoxide ($Zr(OC_3H_7)_4$), 98 % purity; $Sr(NO_3)_2$ 99 %, methylene blue, CH_3COOH 99 %, ethylene diamine tertra acetic acid (EDTA) 99.5 %, ethane 1,2-diol ($HOCH_2CH_2OH$), 99 %, and citric acid ($H_3C_6H_5O_7$) 99%were purchased from Sigma Aldrich.C_2H_5OH (99.5 %; S.G = 0.7951 g/mL), H_2SO_4 (98 %, S.G = 1.84 g/mL), H_2O_2 (30 %), and acetone (99 %; S.G = 0.789–0.792 g/mL were purchased from Guangdong Guang Sci. Tech-Co. Ltd, China(BDH).

2.2. Synthesis of $SrZrO_3$nanoparticles

The Sol-gel Pechini method was used to prepare $SrZrO_3$ [27]. Firstly, 5 mL zirconium iso-propoxide (Zr-*n*-p) was reacted with 0.5 M (40 mL) citric acid under constant stirring for 2 h at 37 °*C*. Thereafter, the temperature was increased to 80 °*C* to aid dissolution. Secondly, in another beaker, 20 mL (0.1 M) of $Sr(NO_3)_2$ was reacted with 22 mL of 0.5 M EDTA dissolved in 25 % NH_3 solution. The Sr-EDTA solution was stirred for 2h at 60 °*C* then, added to Zr^{+4} citrate solution with continuous stirring and heated to 100 °*C* for 2 h. Next, was the addition of 23 mL ethane 1, 2-diol to EDTA - citric acid to the complex. The temperature was raised to 120 °*C* to promote gel formation. The gel was dried at 400 °C for 4 hand further annealed at 800 °C for 2 h. The synthesized flake was milled into a fine powder using mortar and pestle. The obtained white colored powder was stored in a desiccator for characterization.

2.3. Characterization

The crystal structure was investigated by high-resolution X-ray diffractometer (HR-XRD, PAnalytical X'Pert Pro) operating at 40 kV and 40 mA with Cu K α radiation (1.54060 Å) from 10 to 90 ° (2 θ angle) using a step size of 0.05 ° and a counting time of 0.5 s per step at 25 °*C* [28]. Surface morphology was determined using field-emission scanning electron microscope (FE-SEM, FEI Nova NanoSEM 450) at a voltage of 20 kV. Elemental composition was obtained using energy dispersive X-ray spectrometer (EDX) attached to the

FE-SEM. The FT-IR spectrum was probed between 4000 and 400 cm^{-1} using Agilent Technologies (Carry 630 FTIR) with the processing soft Omic 7.3 to access bond formation. UV–visible spectroscopy was performed using Jenway 7415 in the wavelength range of 200–800 nm to obtain the absorption spectrum of the synthesized perovskite. Bulk density was determined by tapping [29].

2.4. Photocatalytic test

Photocatalytic test was performed in the dark and under artificial light illumination [30]. Artificial irradiation was provided by a 500 W Halogen arc lamp. Dark photocatalytic test was investigated as follows; 200 mg of $SrZrO_3$ was added into 50 mL of 5 mg/L MB. The suspension was cycled under darkness for 1 hat 250 rpm, and 2 mL H_2O_2 was added. Then 5 mL of the suspension was withdrawn for every 30 min and centrifuged at 16000 rpm for 10 min to determine residual MB (mg/L). In a similar way, 200 mg of $SrZrO_3$ was added to 50 mL of 5 mg/L MB in a 250 mL photoreactor mounted on a cyclic vibrator. The suspension was cycled under dark for 1 h, then 2 mL of 2 mM H_2O_2 was added and irradiated with 500 W Halogen arc lamp (Beijing Au Light Technology Co.) with a cutoff filter ($\lambda > 420$ nm) with constant cycling from 0 to 150 min. During the irradiation time, 5 mL of the suspension was withdrawn for every 30 min interval and centrifuged at 16000 rpm for 10 min to monitor the rate of photodegradation. Measurements were performed in triplicates in all cases to reduce result dispersion and improve reliability of data. The residual concentration of MB dye in the suspension was monitored using UV–Visible spectrophotometer [31].The equilibrium concentration (C_e) was evaluated from the slope of the calibration curve. The adsorption capacity (q_t) was calculated using Eq. (1).

$$q_t = \frac{(C_0 - C_e)V}{1000m} \tag{1}$$

where q_t (mg/g) is the amount adsorbed at time t, V (cm^{-1}) is the volume of the solution, and m (g) is the mass of photocatalyst. The percentage photo-degradation efficiency was calculated using Eq. (2).

$$\text{D}\ (\%) = \frac{C_o - C_t}{C_0}\ \text{x}\ 100 \tag{2}$$

where D (%) represents the percentage degradation efficiency, Co and C_t are the initial and concentration, respectively at a given time (mg/L).The concentration of MB dye was evaluated using a five-point calibration curve ranging from 0 to 25 mg/L.

2.5. Reusability studies

Reusability study was carried out as described in Refs. [21,32]. Four adsorption/degradation cycles were carried out in order to examine the reusability tests. In this test, 200 mg $SrZrO_3$ was used repeatedly to degrade 5 mg/L of 50 mL MB for 120 min irradiation under visible light at standard conditions. The progress of the reaction was monitored by measuring the absorbance of aliquot after centrifugation at 664 nm and the percentage degradation calculated. At each cycle, the catalyst was desorbed, washed, dried at 80 ° C and annealed at 800 ° C before reuse.

2.6. Kinetic studies

The experimental data were fitted into Zero-order [33], Psuedo-first order (PFO) [34], Psuedo-second order (PSO) [35], Elovich, Intra particle diffusion [36] and liquid film diffusion kinetic models [37] to investigate the mechanism of adsorption, photo-degradation and rate limiting step.

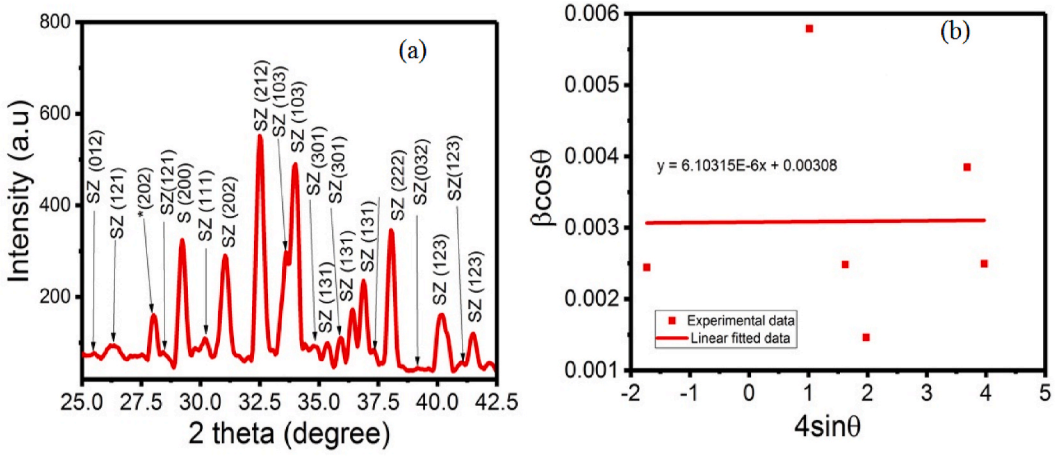

Fig. 1. (a) XRD pattern, (b) Williamson-Hall plot of the $SrZrO_3$nanoparticles.

3. Results and discussion

3.1. Phase analysis

Fig. 1 depicts the XRD pattern of the $SrZrO_3$ nanoparticles treated at 800 °*C* for 2 h. The peaks marked with the prefix SZ could be attributed to the orthorhombic phase of $SrZrO_3$, according to JCPDS card no.01-070-0695 with *Bmmb* 63 space group [38,39].The peaks were sharp, indicating high crystallinity. The peak marked with the prefix 'S' could be traced to the cubic phase of undecomposed strontium from the $Sr(NO_3)_2$ precursor, according to JCPDS card No. 089–4910. The peak marked '*' located at $2\theta = 27.92^{\circ}$ traced to the $SrCO_3$ phase, as also reported by Quinones-Gurrola et al. [40] and Lucena et al. [41].

Peak profile analysis was carried out using Debye Scherrer's (Eq. (3)) and the Williamson-Hall (W–H) method (Fig. 1b and Eqs. (4) and (5)). Alfonso-Herrera et al. [42] reported lower average crystallite size for $SrZrO_3$ annealed in air at 800 °*C* for 8 h. The crystallite size was determined as reported [28,43–46]. The estimated structural parameters are presented in Table 1.

$$D = \frac{k\lambda}{\beta \cos\theta} \tag{3}$$

where D is the Scherer's size or average crystallite size, $\lambda = 0.1541$ nm is wavelength of the X-ray source for Cu k_{α}, β = FWHM (in radians), θ is the Bragg's angle, k is a shape factor numerically equal to 0.9.

$$\beta_{hkl} \cos\theta = \left(\frac{k\lambda}{D_{W-H}}\right) + 4\varepsilon_{W-H} \sin\theta \tag{4}$$

$$D_{W-H} = \frac{k\lambda}{Y_{intercept}} \tag{5}$$

where D_{W-H} is the W–H size or crystallite size, and ε_{W-H} is the Williamson-Hall microstrain determined from W–H plot. The dislocation density, lattice strain and microstrain were determined according to Eqs (6)–(8).

$$\delta = \frac{1}{D^2} \tag{6}$$

$$\varepsilon = \frac{\beta \cos\theta}{4} \tag{7}$$

$$s = \frac{d}{D\sqrt{12}} \tag{8}$$

3.2. Surface morphology

The surface morphology of the sample was recorded at a magnification of × 50,000 (scale of 1 μ m) and is shown in Fig. 2a. The surface looks smooth with irregular shape, in agreement with the result of the bulk density (Table 1). Lower particle size and bulk density enhances high electron-phonon coupling in photocatalyst to prevent charge recombination reactions to enhance photodegradation [47,48].

Table 1
Structural parameters of $SrZrO_3$.

Parameter	Magnitude
2θ	32.52940
FWHM	0.1796
d-spacing	0.2634
Crystallite size (Scherer's method) (nm)	45.56
Crystallite size (W–H method) (nm)	44.50
Microstrain (ε)	1.66×10^{-3}
Lattice strain (ή)	7.49×10^{-4}
Dislocation density (nm^{-2})	4.78×10^{-4}
Bulk density (g/mL)	0.35560
Lattice constants	a = 8.2532
	b = 8.2662
	c = 8.2709
Cell vol. A^3 ($\times 10^6$ p.m.^{3})	564.26
Calculated density (g/cm^3)	5.3400
hkl plane	212

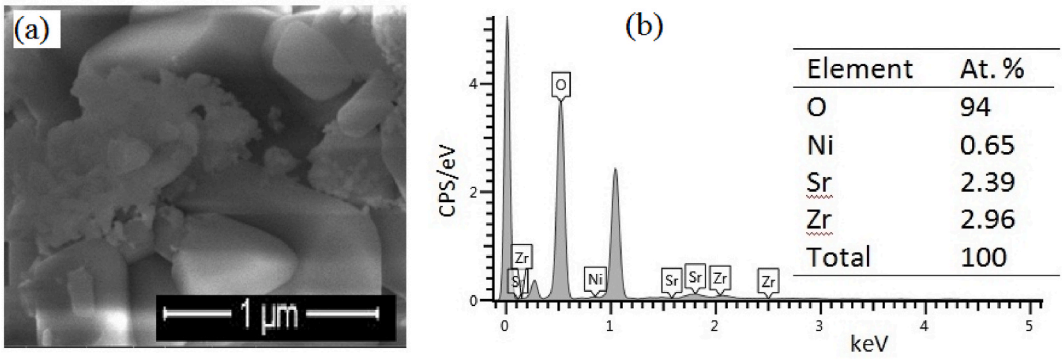

Fig. 2. (a) FESEM image, (b) EDX spectrograph of the $SrZrO_3$ nanoparticles.

3.3. Elemental composition

The chemical composition of the synthesized perovskite was investigated using EDX is shown in Fig. 2b. The spectrograph confirmed the presence of Sr, Zr and O elements in the synthesized $SrZrO_3$ compound, and their equivalent elemental atomic weight percent is shown in the inset of Fig. 2b. The insignificant amount of Ni impurity could be introduced by handling effect.

3.4. Fourier transform infrared spectroscope

The FTIR spectrum of $SrZrO_3$ nanoparticles in the range of 4000-400 cm^{-1} is presented in Fig. 3a. While Fig. 3b showed the zoom FTIR of $SrZrO_3$ nanoparticles. From the Full FTIR spectrum, eleven bands were observed: 3792.34, 3741.75, 3464.84, 3230.92, 3209.58, 2954.31, 2545.55, 2334.61, 1648.43, 1196.99 and 645.57 cm^{-1}. Aravinthkumar et al. [9] and Ouni et al. [49] reported the spectra band positions and absorption peak shift to be influenced by the material composition, lattice constants, microstrain, shape of the material as well as annealing temperature. The bands located at 2545.53 and 2334.61 cm^{-1} could be assigned to carbonate vibrations and indicative of the carbonate group represent the stretching vibration of the asymmetrical C–O bond in the CO_3^{2-} group [9, 35]. The bands above 3000 cm^{-1} could be associated with water angular deformation associated with O–H stretching. This interpretation agrees with the reported by Katyayan and Agrawal [37] who described spectra band range of 3633–3905 cm^{-1} to minute traces of moisture (O–H). Triyono et al. [50] also reported the bands above 2000 cm^{-1} (O–H bond) to stretching vibrations of absorbing ambient moisture. In addition, Perumal et al. [51] and Pan et al. [52] described the broad band around 3426 cm^{-1} and above to be associated to O–H stretching vibration and bending mode of water molecules due to the O–H/H_2O functional group present in the prepared catalysts due to atmospheric water vapour on the surface of the catalyst. The absorption bands peak at 1648.43–1196.99 cm^{-1} may be associated with the carbonyl group (C═O) from the chelating precursors.

The mode of metal-oxygen (Sr–O) bond vibration of the synthesized compound was centered at approximately 648.35 cm^{-1} (Fig. 3b), indicating the formation of the perovskite structure [35]. This result is consistent with the finger print region for metal-oxygen bond in the wavenumber range of 400–600 cm^{-1} reported in the literatures [37,51].

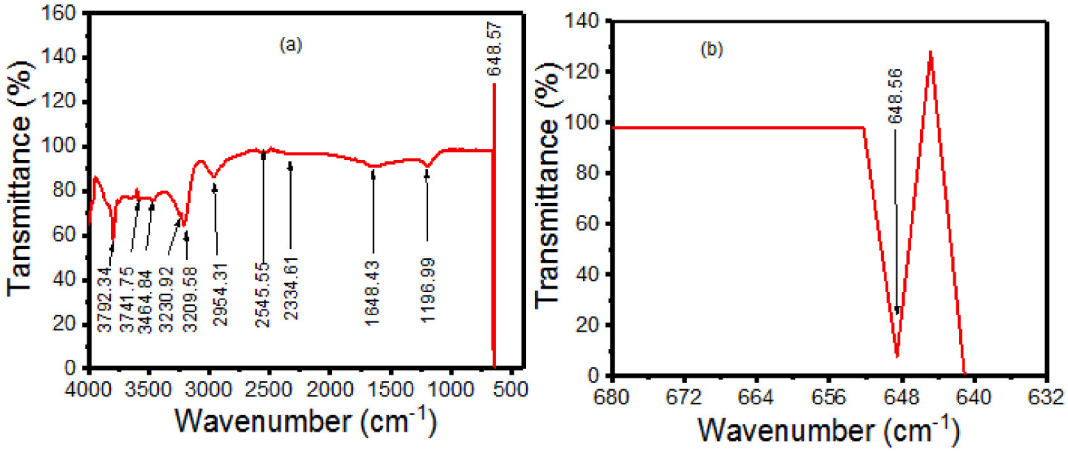

Fig. 3. (a) FTIR Spectrum of $SrZrO_3$ nanoparticles, (b) Zoomed-in image of the FTIR result.

3.5. Optical properties

Fig. 4a depicts optical absorption spectrum of the $SrZrO_3$. A high optical absorbance could be observed near the absorption edge in the UV region, suggesting that the sample is sensitive to UV light. Fig. 4b displays the graph of $(\alpha\ h\nu)^2$ against photon energy ($h\nu$) for the estimation of optical band gap energy. The band gap energy determined in accordance with Tauc formula (Eqn. (9)) was 5.31 eV [53,54]. The optical band gap energy obtained agrees with the report of Cabello et al. [55]. Aside other physical and chemical properties of nanomaterials, the change in the optical band gap energy could be due to various effects such as doping, synthesis technology, strain, particle morphology, annealing temperature, concentration of precursors, solution pH and reactions conditions [23,51,56,57].

$$\alpha h\nu = C\left(h\nu - E_g\right)^m \tag{9}$$

where E_g is the optical bandgap energy, $h\nu$ is the photon energy, C is a constant, and m is a factor that depends on the type of allowed electronic transition and is numerically equal to $\frac{1}{2}$ for a direct allowed electronic transition.

3.6. Methylene blue linear fit

A five-point linear fit for MB was obtained to study the photodegradation (Fig. 5a). The fit was obtained using 5–25 mg/L concentration of MB. To establish the fit, the absorbance of these concentrations was obtained at 664 nm (the absorption maximum of MB) and plotted against the concentrations to obtain a linear regression equation used to estimate the equilibrium concentration of degraded MB.

3.7. Degradation studies

3.7.1. Time-dependent absorption spectrum

The result of time-dependent absorption spectrum for the effect of light is shown in Fig. 5b. It was observed that absorbance decrease with increase in time of irradiation at 200 mg of catalyst dosage in 50 mL of 5 mg/L MB dye from 30 to 150 min. The increase in irradiation time changes the color of the suspension to lighter-blue, which is responsible for the bond cleavage of the chromophoric group present in the dye solution [21]. The progress of the reaction was followed by monitoring the decrease in the absorbance of methylene blue at $\lambda_{max} = 664$ nm.

3.7.2. Absorbance and degradation studies in the dark and light illumination

Fig. 6a illustrates the absorbance plot obtained in the dark and light illumination reactions for MB dye degradation using $SrZrO_3$ assisted H_2O_2. The initial absorbance (0.189) for MB in the dark did not decrease. However, in the presence of light irradiation the absorbance was observed to decrease from 0.189 to 0.080 between the time intervals of 0–150 min. This is an indication that photodegradation occurred. Fig. 6b shows the photodegradation efficiency of MB. The degradation efficiency in the dark and in the presence of light irradiation was 35 % and 80 %, respectively, in the time interval of 30–150 min. This observation showed that photocatalytic degradation of MB was enhanced by increasing the reaction time. Alammar et al. [58] reported degradation efficiencies of 45, 30 and 45 % for MB for 80 min reaction time using prestine $SrTiO_3$, $CaTiO_3$ and $BaTiO_3$ perovskites irradiated with high pressure Hg lamp using10 mg/L of MB and 100 mg catalyst. Bellam et al. [59] reported 60 % degradation efficiency of MB within 150 min reaction time using N_2 doped $NiTiO_3$ irradiated with visible light using 3.2 mg/L of MB.

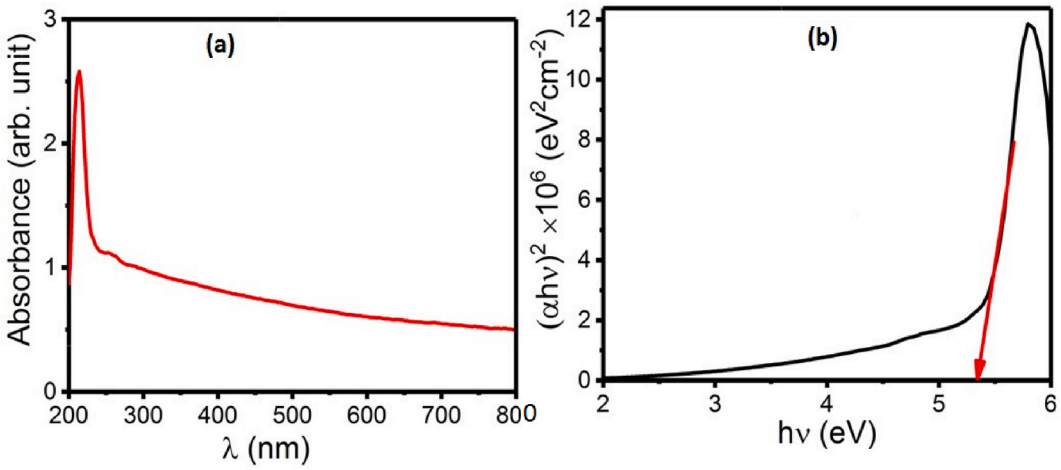

Fig. 4. (a) Optical absorption spectrum, (b) Tauc plot of the $SrZrO_3$.

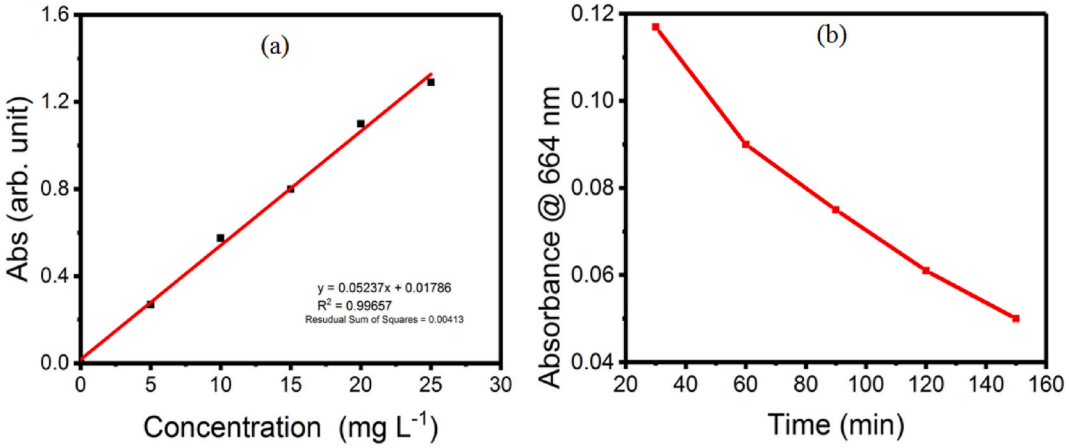

Fig. 5. (a) Linear fit of MB dye, (b) Time-dependent absorption spectrum.

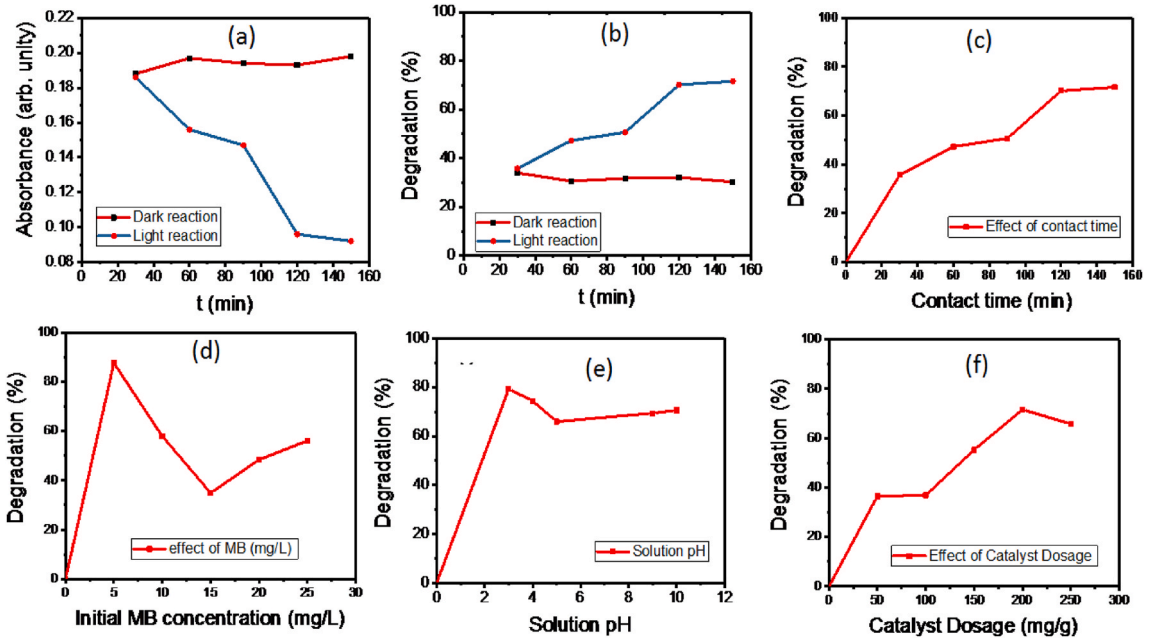

Fig. 6. Effect of photodegradation parameters on MB (a) absorbance, (b) Degradation efficiency, (c) Contact time, (d) Initial MB concentration, (e) Solution pH and, (f) Catalyst dosage.

3.7.3. Adsorption kinetics

The efficiency of $SrZrO_3$ catalyst for the degradation of MB from aqueous solution was investigated using a batch equilibrium technique by using different amounts of catalyst in a reaction vessel containing 50 mL of MB. The adsorption kinetic studies were studied for different pH values, contact time, catalyst dosage and MB dye concentration.

3.7.4. Effect of contact time

The effect of contact time on degradation efficiency was examined using 50 mL of 5 mg/L MB and 200 mg catalyst from 0 to 150 min. Fig. 6c showed that an increase in the contact time led to a decrease in residual MB concentration. The highest removal efficiency was observed at 120 min. There is no previous work on the use of $SrZrO_3$ and $SrZrO_3$ coupled H_2O_2 for which we can compare the present report. Nevertheless, the effect of contact time on degradation efficiency of MB using various catalysts could be found in the literatures. Soltanabadi et al. [60] reported the removal of rhodamine B (30 mg/L; V = 100 mL) within 90 min using visible light irradiation with assisted H_2O_2 for $LaFeO_3$ supported CuO. The performance of H_2O_2 for $LaFeO_3$was higher compared to the pure $LaFeO_3$, thus, supporting the good performance observed for our $SrZrO_3$ supported H_2O_2. In a related study, Chang and Hu [61] reported over 70 % degradation efficiency for MB, methyl orange, Rhodamine, bisphenol A and phenol using $SrTiO_3$ supported 20 wt%

Ga_2O_3 within 3 h irradiation.

3.7.5. Effect of initial MB concentration

The initial dye concentration is another important variable that can affect adsorption process. The effect of initial MB concentration on degradation efficiency was investigated by varying the initial MB concentration from 5 to 25 mg/L, using catalyst dosage of 200 mg and contact time of 0–150 min. Results showed decreased degradation efficiency of MB with increasing initial MB concentration (Fig. 6d). This behavior could be attributed to the oversaturation of the available photocatalyst active sites [62]. Higher adsorption of pollutant with a high initial concentration of pollutant facilitates more pollutant molecules to get excited on light irradiation, which enhances the photodegradation efficiency. However, at higher concentration reduction in photodegradation is observed due to reduction in the number of photons reaching onto the surface and consequent reduction in the number of OH* radicals and positive hole generation [63].

3.7.6. Effect of pH

The effect of initial solution pH on degradation and removal efficiency was evaluated at pH 3–10, while the initial MB concentration and catalyst dosage were fixed at 5 mg/L and 200 mg, respectively. The degradation efficiency was found to be 80 % in acidic pH 3 and decreased with increase in pH (Fig. 6e). This could be due to surface electrostatic charge, oxidative potential and sorption capacity between the dye molecule and $SrZrO_3$ nanoparticles surface [64,65]. Yazdanbakhs*ket al.* [66] reported pH 2 as the optimum pH for the removal of Reactive blue 5 dye from aqueous solution containing Ca doped lanthanum nickel trioxide catalyst.

3.7.7. Effect of catalyst dosage

Fig. 6f showed the effect of catalyst dosage. The degradation efficiency was highest at 200 mg. At higher dosage, the degradation was found to decrease. One of the possible reasons might be the turbidity of the solution, which increased with the amount of catalyst and blocked the photons reaching the medium. This phenomenon may result to a smaller number of active photoactive species and consequently reduction in percentage of degradation. Several studies report the photocatalytic rate to first rise along with catalyst loading and then deflate at high dosage due to unavailable active surface sites for exposure and light scattering effects [67].

3.7.8. Reusability studies

The photocatalytic reusability of the synthesized photocatalyst was investigated via stability test. The photocatalytic reusability test of the photocatalyst was studied for MB degradation up to four cycles (Fig. 7). The degradation efficiency of MB was slightly decreased during the four consecutive cycles. The decrease in degradation efficiency could be attributed to the catalyst loss with each cycle due to the procedural approach [18]. The decrease in quantity of the catalyst during processing for reusability could be traced to the reduction in the numbers of active cites (adsorbent) in the MB dye.

3.8. Kinetic models

The models used for describing the experimental data were the Zero-order, PFO, PSO, Elovich, Weber-Morris and Liquid Film Diffusion kinetic rate models [37]. These models were applied to determine the one that best described the uptake and degradation of MB dye in solution. Fig. 8a shows the experimental and fitted plots of Zero-order kinetic model for the effects of catalyst dosage, initial MB concentration and solution pH 3. Mesbah et al. [68] described R^2 as a viable tool for judging the fitness of a kinetic model. The R^2 values derived from the Zero-order kinetic model is presented in Table 2. The R^2 value for the effect of dosage was the highest, indicating lower values of error functions. In addition, values of calculated adsorption equilibrium capacity ($q_{e(cal)}$) were noticed to be

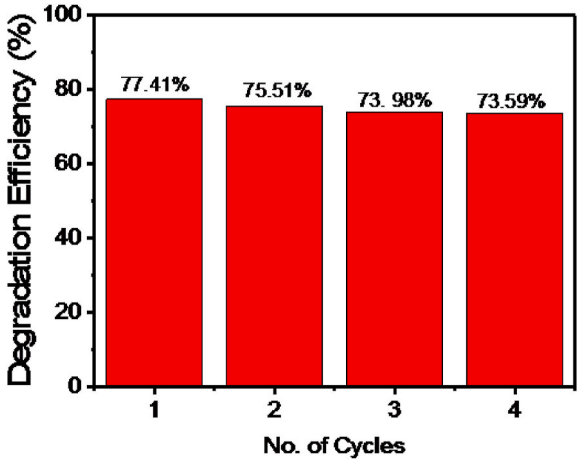

Fig. 7. Degradation efficiency of MB at four consecutive cycles.

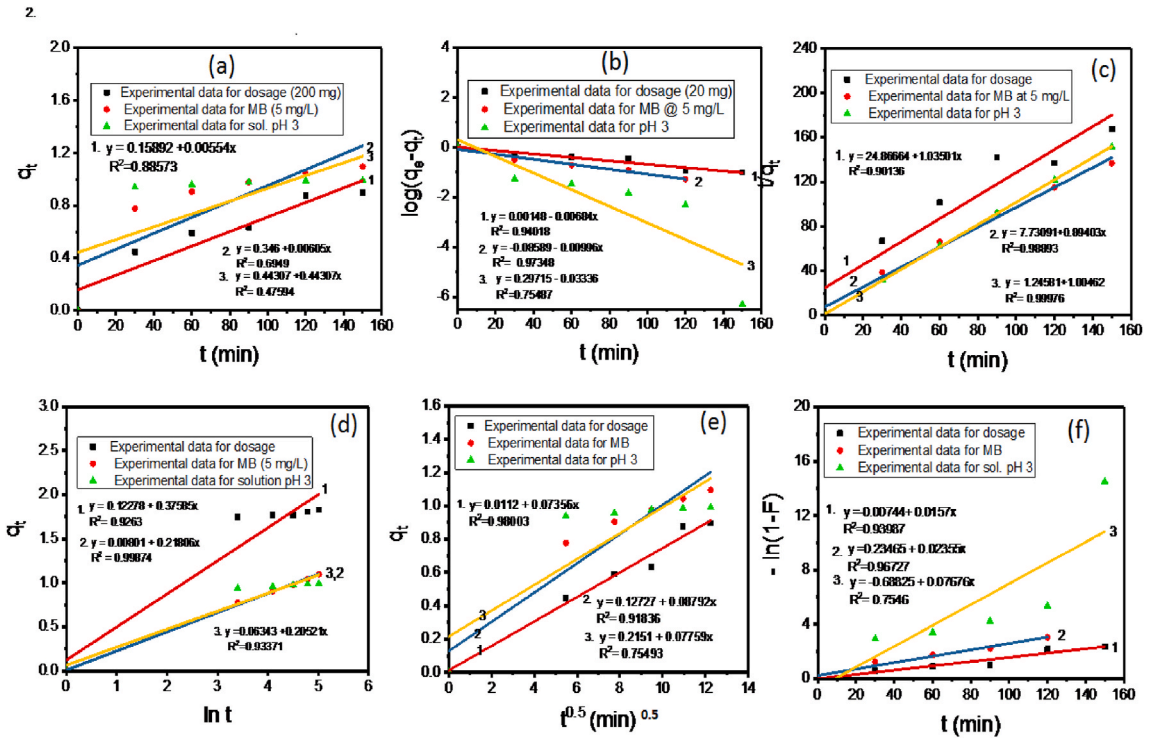

Fig. 8. Experimental and linear fits for the effects of dosage, initial MB concentration and pH 3 for, (a) Zero-order, (b) PFO, (c)PSO, (d) Elovich, (e) Weber-Morris, (f) Liquid film diffusion model for the degradation of MB at 30 °C.

lower than the experimental adsorption equilibrium capacity $q_{e(exp)}$. The result of the half-life ($t_{1/2}$) and equilibrium constant for zero-order (k_0) were negative for all the experimental variables, signifying that the experimental data did not fit into this model. Therefore, there is need to test other models that may fit best.

The experimental and fitted plots for the PFO kinetic model were shown in Fig. 8b. The regression values are presented in Table 3. The R^2 value was maximum at the initial MB concentration (5 mg/L), while the lowest was found for the effect of solution pH 3. Further to this, the $q_{e(cal)}$ values for dosage and solution pH 3 were higher than the $q_{e\ (exp)}$ values. Comparing the results in Tables 2 and 3, it could be observed that the PFO model exhibited higher R^2 and $q_{e(cal)}$ values compared to the Zero-order model, suggesting that the PFO model performed better than its counterpart. However, the PFO model like the Zero-order model did not fit well into the absorption process, hence the need to exploit the PSO kinetic model.

The PFO rate constant (k_1) for the effects of solution pH 3 was highest compared to the effect of dosage and initial MB concentration. This means that at this pH most of the MB change to zwitter ionic form and resulted in the increased adsorption capacity (Table 3) of MB onto the surface of $SrZrO_3$ and consequently, increase rate of degradation. In addition, the fractional power defined as the ratio of q_t/q_e per unit time was highest for the effect of initial MB concentration. This suggested that at this concentration more MB was adsorbed on the photocatalyst.

The results of the linear plots and the kinetic parameters for the PSO model were shown in Fig. 8c and Table 4, respectively. The coefficient of determination for the variables was nearly unity suggesting that the reaction followed a second order rate constant with higher efficiency. The equilibrium constant (K_2) was highest at solution pH 3 signifying that more MB was adsorbed with subsequent degradation. The $t_{1/2}$ for the degradation efficiency was observed to be 2 min, suggesting that the data corresponds to the initial sorption rate. The $q_{e(cal)}$ values were higher than the $q_{e(exp)}$, suggesting that all the investigated parameters fit well into the PSO model. The fractional power (q_t/q_e) for the variables was estimated to be 0.660, 0.916 and 0.922 for the effect of dosage, MB concentration and solution pH, respectively, suggesting that the MB adsorption rate on the $SrZrO_3$ catalyst was proportional to the available sites.

The linear fit for the Elovic kinetic model was depicted in Fig. 8d. The result indicated a near unity of R^2 for the initial MB concentration (Table 5). The initial sorption rate (α) was highest for catalyst dosage, implying that the adsorption of MB dye on the surface

Table 2
Kinetic parameters of Zero-order model.

Parameter	R^2	$q_{e(cal)}$	$q_{e(exp)}$	K_0	$t_{1/2\ (min)}$
Dosage	0.8857	0.1589	0.9916	−0.0055	−451.26
MB (mg/L)	0.6949	0.3460	1.0966	−0.0061	−413.22
Solution pH	0.4759	0.4431	0.9916	−0.4431	−5.68

Table 3
Kinetic parameters of PFO model.

Parameter	R^2	$q_{e(cal)}$ (mg/g)	$q_{e\ (exp)}$ (mg/g)	k_1 (min^{-1})	$t_{1/2}$ (min)	$\frac{q_t}{q_{e\ (cal)}}$
Dosage (mg)	0.9402	1.0034	0.9916	0.0158	43.99	0.6509
MB (mg/L)	0.9735	0.8206	1.0966	0.0230	30.22	0.9014
Solution pH 3	0.7549	1.9822	0.9916	0.0768	9.02	0.9006

Table 4
Kinetic parameters of PSO model.

Parameter	R^2	$q_{e(cal}$ (mg/g)	$q_{e\ (exp)}$ (mg/g)	k_2 (min^{-1})	$t_{1/2}$ (min)	ISR (min^{-1})
Dosage	0.9103	0.9662	0.9916	0.0431	4.64	0.0402
MB (mg/L)	0.9889	1.1185	1.0966	0.1034	1.93	0.1293
Solution pH	0.9998	0.9954	0.9916	1.0093	0.20	1.0000

Note: ISR is initial sorption rate.

of $SrZrO_3$ was > 50 %. The fractional surface coverage (θ) for the effect of MB obtained was the highest (Table 5), this is similar to the report of Kajitvichyanukul and Ananpattarachai [37], hence suggesting a good adsorption and degradation process.

Fig. 8e illustrated the linear fits for the Weber-Morris Kinetic model. Catalyst dosage has the highest coefficient of determination, R^2, suggesting less error values (Table 6). The rate of diffusion coefficient (k_{id}) was highest for the effect of concentration. The initial adsorption (β) was highest for solution pH 3, indicating that the process was pH dependent.

Fig. 8f illustrated the linear fits of Liquid film diffusion kinetic model. The kinetic parameters for the model are shown in Table 7. The equilibrium constant (k_{fd}) for the sorption was negative indicating a non-film diffusion of the adsorbate through the photocatalyst [33].

3.9. Nonlinear error functions analysis

Studies have shown that the error structure of experimental data is usually changed during the transformation of adsorption kinetics into their linear forms [5]. It is for this reason that nonlinearized regression analysis become inevitable, since it provides a mathematical rigorous method for determining kinetic adsorption parameters using original form of kinetic equations. Unlike linear regression, the nonlinear regression usually involves the minimization of error distribution between the experimental data and the predicted kinetic model based on convergence criteria. The following nonlinear error functions were calculated: sum square of errors (ERRSQ), hybrid fractional error function (HYBRID), average relative error (ARE), marquardt's percent standard deviation(MPSD), sum of absolute errors (EABS), standard error (SE), nonlinear chi-square test (χ^2), sum of absolute error (SAE), sum of relative error (S_{RE}), percentage standard deviation (Δq %) and coefficient of non-determination (1-R^2) [69].

Table 8 depicts the result of the nonlinear error analysis for zero-order kinetic. The nonlinear error calculated using HYBRID method was highest for solution pH 3, MB concentration and dosage. It was also observed that errors due to HYBRID calculations were higher for the highest dosage. Hence, it was better at lower catalyst concentration.

Table 9 shows the results of the nonlinear error functions for the PFO kinetic model. The error functions are very high indicating that the sorption did not follow the PFO model.

Table 10 shows the result of nonlinear errors for the PSO kinetic model. The error values for ERRSQ, HYBRID, MPSD, SE, S_{RE} and χ^2 decreased down the table for the effect of dosage, MB concentration and solution pH 3.

It should be noted that error function analysis was not conducted on the results of Elovich, Weber-Morris and Liquid film diffusion models. Nonetheless, the nonlinear adsorption kinetics result for the zero-order, PFO and PSO revealed that the PSO kinetic model best described the kinetic experimental data with lower error values. This finding is similar to a literature report on the nonlinear error functions for adsorption of fluoride on $LaFeO_3$ photocatalyst [68].

3.9.1. Proposed reaction scheme for the photodegradation of MB using $SrZrO_3$ nanoparticles coupled H_2O_2

The photodegradation of MB dye in presence of $SrZrO_3$ couple H_2O_2 could be attributed to the combined effects of dissociation of H_2O_2 in the presence of light and the complex transport of highly reactive hydroxyl radical (*OH) in the reactant mixture. Chiou et al. [70] and Saha et al. [71] proposed the following reaction schemes:

$$H_2O_2 + h\nu \rightarrow 2^{*}OH \tag{10}$$

$$h\nu^{+} + OH^{-} \rightarrow {}^{*}OH \tag{11}$$

$$e^{-} + H_2O_2 \rightarrow {}^{*}OH + OH^{-} \tag{12}$$

Table 5
Kinetic parameters for the Elovic model.

Parameter	R^2	1/β	β	α (g/mg.min^2)	θ
Dosage	0.9263	0.3758	2.6606	0.5211	0.3693
MB (mg/L)	0.9987	0.2181	4.5859	0.2262	0.8772
Solution pH	0.9337	0.2052	4.8731	0.2795	0.7589

Table 6
Kinetic parameters of Weber-Morris model.

Parameter	R^2	k_{id} (mg.g^{-1}min^{-1})	β (mg/g)
Dosage	0.9800	0.0736	0.0112
MB (mg/L)	0.9184	0.0879	0.1273
Solution pH	0.7549	0.0776	0.2151

Table 7
Kinetic parameters for Liquid film diffusion model.

Parameter	R^2	k_{fd} (mg g^{-1} min^{-1})	Intercept
Dosage	0.9399	−0.0157	−0.0074
MB (mg/L)	0.9673	−0.0236	0.2347
Solution pH	0.7546	−0.0768	−0.6883

Table 8
Nonlinear error values for the zero-order kinetic model.

Parameter	ERRSQ	HYBRID	ARE	MPSD	SAE	SE	Δq (%)	S_{RE}	χ^2	1-R^2
Dosage	0.6933	69.918	−16.79	0.8397	0.833	0.372	41.99	8.814	4.362	0.0617
MB (mg/L)	0.5634	51.374	−13.68	0.6845	0.751	0.335	34.22	7.220	1.628	0.0321
Soln. pH	0.3008	30.339	−11.06	0.5532	0.548	0.245	27.66	5.806	0.679	0.0576

Table 9
Nonlinear error functions for the PFO kinetic.

Parameter	ERRSQ	Hybrid	ARE	MPSD	SAE	SE	Δq (%)	S_{RE}	χ^2	1-R^2
Dosage	0.0001	0.0142	0.239	0.012	0.012	0.005	0.598	0.126	0.000	0.0998
MB (mg/L)	0.0762	6.9474	−5.034	0.252	0.276	0.123	12.59	2.655	0.069	0.0176
Soln. pH	0.0001	0.0142	0.239	0.012	0.012	0.005	0.598	0.126	0.000	0.0998

Table 10
Nonlinear error functions for the PFO kinetic model.

Parameter	ERRSQ × 10^{-4}	Hybrid	ARE	MPSD	SAE × 10^{-2}	SE	Δq (%)	S_{RE}	χ^2 × 10^{-4}	1-R^2 ×10^{-2}
Dosage	6.00	0.0649	−0.5119	0.026	2.00	0.011	1.280	0.269	6.00	8.9
MB (mg/L)	5.00	0.0438	0.3999	0.020	−2.00	0.010	0.100	0.211	4.00	0.005
Soln. pH 3	0.15	0.0015	0.0777	0.004	0.40	0.002	0.194	0.041	0.15	0.3

$$h^+ + OH^- \rightarrow {}^{*}OH \quad (13)$$

$$e^- + O_2 \rightarrow {}^{*}O_2^- \quad (14)$$

$$RH + {}^{*}OH \rightarrow H_2O + CO_2 \quad (15)$$

The first step involves the direct photolysis of H_2O_2 to produce hydroxy radical (Eq. (10)) as a crucial step in improving the rate of photocatalytic reaction. Saha et al. [72] suggest that H_2O_2 is a better electron acceptor than oxygen. This phenomenon decreases the chances of electron-hole (e^--h^+) recombination. In Eqs. (11)–(13) the hydroxyl ion reacts with the holes generated during excitation to produce hydroxyl radical while the electron at the conduction band react with the more H_2O_2 ion to produce more hydroxyl radical and ion simultaneously, which in turn reduced the probability of e^--h^+ recombination. The superoxide radical ($^{\bullet}O_2^-$) as indicated in Eq.

(14), is less dominant in affecting the rate of photocatalytic reaction as compared with hydroxyl radicals [70]. In Eq. (15), the organic dye (methylene blue) RH, react with the hydroxyl radical to produce carbon dioxide, water and intermediates. In addition, the surface reaction of H_2O_2 on the surface of $SrZrO_3$ catalyst may be represented in Eqs. (16)–(20) [73,72].

$$C^+ + H_2O_2 \rightarrow C^+ + H^+ + HO_2^- \ (C^+ = \text{Oxidized catalyzed surface}) \quad (16)$$

$$C + H_2O_2 \rightarrow C + {}^{*}OH + OH^- \ (C = \text{Reduced catalyzed surface}) \quad (17)$$

$$C^+ + O_2^- \rightarrow C + O_2 \quad (18)$$

$$C + {}^{*}OH_2 \rightarrow C + HO_2^- \quad (19)$$

$$C + {}^{*}OH \rightarrow C^+ + OH^- \quad (20)$$

It is obvious that in these model equations, H_2O_2 may react with both oxidized and reduced catalyst surface (Eqs. (7) and (8)) and both the catalyst and H_2O_2 undergo simultaneous redox reaction. This resulted to generation of more hydroxyl radicals and ions that may, in turn, act as e^--h^+ scavengers to react with the organic molecules. The hydroxyl radicals, to a large extent, play important role in the photocatalytic oxidation process, and in photodegradation of Methylene blue dye. Therefore, the effect of the addition of hydrogen peroxide will yield more hydroxyl radicals in the process hence a better photocatalytic reaction [74,75]. As shown in Eqs. (18)–(20), superoxide, hydroxyl and perhydroxyl radicals reacted on the catalyst surface to further enhance the photocatalytic activity.

4. Conclusion

$SrZrO_3$ perovskite was synthesized by the sol-gel Pechini method and annealed at 800 $^{\circ}C$ for 2 h. The sample was characterized using XRD, FE-SEM, FTIR, EDX and UV–visible spectrophotometer. The prepared $SrZrO_3$ perovskite exhibited orthorhombic phase. Debye Scherrer and Williamson-Hall crystallite size were found to be 45.56 and 44.50 nm, respectively. The FESEM images showed microstructures with a smooth surface. The EDX result confirmed the presence of the constituent elements. The optical band gap was estimated to be 5.31 eV. Photodegradation of the MB using $SrZrO_3$ coupled H_2O_2 was enhanced in visible light irradiation compared to dark reactions. Photocatalytic activity was investigated for the effects of time, catalyst dosage, adsorbate concentration and solution pH. The optimized time for the degradation studies was 150 min. The degradation efficiency was greater than 80 % under visible light and lower than 40 % in the dark. The experimental data were fitted into Zero-order, Pseudo-first order, pseudo-second order, Elovic, intraparticle diffusion and Liquid-film diffusion kinetic models. The experimental data fitted best into PSO kinetic model due to the higher values of coefficient of determination. Nonlinear error functions were calculated for the various kinetic models to determine lower values of error functions, where the Psuedo-second order kinetic model demonstrated lower values of error functions.

Data availability

The data used for this paper will be made available on request.

CRediT authorship contribution statement

J.N. Tsaviv: Writing – original draft, Visualization, Software, Resources, Methodology, Investigation, Data curation, Conceptualization. **I.S. Eneji:** Writing – review & editing, Visualization, Validation, Supervision, Methodology, Conceptualization. **R. Sha'Ato:** Writing – review & editing, Visualization, Validation, Supervision, Methodology, Conceptualization. **I. Ahemen:** Writing – review & editing, Visualization, Validation, Supervision, Methodology, Conceptualization. **P.R. Jubu:** Writing – review & editing, Software, Formal analysis. **Y. Yusof:** Software, Formal analysis.

Declaration of competing interest

The authors declare that they have no known competing financial interests or personal relationships that could have appeared to influence the work reported in this paper.

Acknowledgements

The authors sincerely thank Universiti Sains Malaysia for the Short-Term Grant (No. 6315379) for materials characterization.

References

[1] S.P. Goutam, G. Saxena, V. Singhm, A.K. Yadav, R.N. Bharagava, Kh B. Thapa, GreenSynthesis of TiO_2 nanoparticles using leaf extract of *Jatropha curcas L.* For photocatalytic degradation of tannery wastewater, Chem. Eng. J. 336 (2018) 386–396.

[2] N. Nakada, S. Hanamoto, M.D. Jürgens, A.C. Johnson, M.J. Bowes, H. Tanaka, Assessing the population equivalent and performance of wastewater treatment through the ratios of pharmaceuticals and personal care products present in a river basin: application to the River Thames basin, UK, Sci. Total Environ. 575 (2017) 1100–1108.

[3] P. Kay, S.R. Hughes, J.R. Ault, A.E. Ashcroft, L.E. Brown, Widespread routine occurrence of pharmaceuticals in sewage effluent, combined sewer overflows and receiving waters, Environ. Pollut. 220 (2017) 1447–1455.
[4] P. Mehdizadeha, O. Amirib, S. Rashkic, M. Salavati-Niasaria, M. Salimiand, L.K. Foong, Effective removal of organic pollution by using sonochemical prepared $LaFeO_3$ perovskite under visible light, Ultrason. Sonochem. 61 (2020) 104848.
[5] C. Byrne, G. Subramanian, C.S. Pillai, Recent advances in photocatalysis for environmental applications, J. Environ. Chem. Eng. 6 (2018) 3531–3555.
[6] S. Rajagopal, B. Paramasivam, K. Muniyasamy, Photocatalytic removal of cationic and anionic dyes in the textile wastewater by H_2O_2 assisted TiO_2 and micro-cellulose composites, Separ. Purif. Technol. 252 (2020) 117444.
[7] J. Kong, T. Yang, Z. Rui, H. Ji, Perovskite-based photocatalystsfor organic contaminants removal: current status and future perspectives, Catal. Today 327 (2018) 47–63.
[8] E. Grabowska, Selected perovskite oxides; characterization, preparation and photocatalytic properties, Appl. Catal., B 186 (2016) 97–126.
[9] L. Aravinyhkumar, I.J. Peter, G.A. Babu, M. Navaneethan, S. Karazhanov, C.R. Mohan, Enhancing the Short circuit current of a dye-sensitized solar cell abd photocatalytic dye degradation using Cr-doped $SrTiO_3$ interconnected spheres, Mater. Lett. 319 (2022) 132284.
[10] K. Aravinyhkumar, e. Praveen, A.J.R. Mary, C.R. Mohan, Investigation on $SrTiO_3$ nanoparticles as a photocatalyst for enhanced photocatalytic activity and photovoltaic applications, Inorg. Chem. Commun. 140 (2022) 109451.
[11] K. Ashish, K. Ajay, K. Venkata, Perovskite oxide based materials for energy and environment oriented photocatalysis, ACS Catal. 10 (2020) 10253–10315.
[12] A. Khataee, S. Arefi-Oskoui, M. Fathinia, A. Fazli, A.S. Hojaghan, Y. Hanifehpour, S.W. Joo, Photocatalysis of sulfasalazine using Gd-doped PbSe nanoparticles under visible light irradiation: kinetics, Intermediate Identification and Phyto-toxicological Studies, J. Ind. Eng. Chem. 30 (2015) 134–146.
[13] H. Jiang, J. He, C. Deng, X. Hong, B. Liang, Advances in Bi_2WO_6-based photocatalysis for degradation of organic pollutants, Molecules 27 (2022) 8698.
[14] M.L. Rojas-Cervantes, E. Castillejos, Perovskites as catalysts in advanced oxidation processes for wastewater treatment, Catalysis 9 (2019) 230–268.
[15] Y. Hu, L. Mao, X. Guan, K.A. Tucker, H. Xie, X. Wu, J. Shi, Layered perovskite oxides and their derivative nanosheets adopting different modification strategies towards better photocatalytic performance of water splitting, Renewable Sustainable Energy Rev. 119 (2020) 109527.
[16] K. Wei, Y. Faraj, Yao, R. Xie, B. Lai, Strategies for improving perovskite photocatalysts reactivity for organic pollutants degradation, Chem. Eng. J. 414 (2021) 128783.
[17] S. Porcu, F. Secci, P.C. Ricci, Advances in hybrid composites for photocatalytic applications, Molecules 27 (2022) 6828.
[18] S. Janaki, K. Punithamurthy, L. Renuka, A Novel approach for synthesis of $LaFeO_3$/Bentonite Nanocomposite for degradation of methylene blue with enhanced photocatalytic activity', Mater. Res. Express 6 (2019) 035013.
[19] Y.X. Yan, H. Yang, Z. Yi, R.S. Li, T. Xian, Design of ternary $CaTiO_3$/g-C_3N_4/AgBr Z-scheme heterostructured photocatalysts and their application for dye photodegradation, Solid State Sci. 100 (2020) 106102.
[20] X. Zhou, Y. Chen, C. Li, L. Zhang, X. Zhang, X. Ning, L. Zhan, J. Luo, Construction of $LaNiO_3$ nanoparticles modified g-C_3N_4 nanosheets for enhancing visible light photocatalytic activity towards tetracycline degradation, Sep. Purif. Technol. 211 (2019) 179–188.
[21] K. Aravinyhkumar, G.A. Babu, C.R. Mohan, Promoting active sites of Fe^{3+} ions in $SrTiO_3$ nanosphere: a superior candidate for high performances of dye –sensitized solar cell and photocatalytic dye degradation, Colloids Surf. A Physicochem. Eng. Asp. 672 (2023) 131702.
[22] K. Ramakrishnan, V. Gayathri, K. Aravinyhkumar, K. Ramachandran, B. Ajitha, M. Rameshbabu, S. Sasiflorence, S. Karazhanov, K. Praba, C.R. Mohan, TiO_2/CeO_2 core/shell nanostructures for photocatalytic and photoelectrochemical applications, Inorg. Chem. Commun. 144 (2022) 109842.
[23] J.R. Alvarez-Corena, J.A. Bergendahl, F.L. Hart, Advanced oxidation of five contaminants in water by UV/TiO_2: reaction Kinetics and by-products identification, J. Environ. Manag. 181 (2016) 544–551.
[24] A.M. Huerta-Flores, L.M. Torres-Martínez, D. Sánchez-Martínez, M.E. Zarazúa-Morín, $SrZrO_3$ powders: alternative synthesis, characterization and application as photocatalysts for H_2 evolution from water splitting, Fuel 158 (2015) 66–71.
[25] A. Nathan-Abutu, I. Ahemen, A. Reyes-Rojas, Structural and optical investigation of novel $Sr_{1-x}Na_{2x}ZrO_3$Perovskite nanoparticles, Physica B 653 (2023) 414655.
[26] K. Ashish, K. Ajay, K. Venkata, Perovskite oxide based materials for energy and environment oriented photocatalysis, ACS Catal. 10 (2020) 10253–10315.
[27] R.C. Andrades, A.H.M. Júnior, L.F. de Miranda, R.A. Rocha, Preparation and characterization of $Pb(Zr,Ti)O_3$ obtained by the Pechini method, Mater. Sci. Forum 912 (2018) 97–101.
[28] P.R. Jubu, F.K. Yam, K.T. Low, Feasibility study on synthesis of G_2O_3 nanostructures on glass substrate by chemical vapor deposition, Thin Solid Films 10 (2020) 1–7.
[29] I.S. Eneji, N. Julian, R. Sha'Ato, Kinetic and thermodynamic study of aqueous adsorption of Cd^{2+} and Pb^{2+} ions on activated carbon from *Nymphaea ampla* (water lily) roots, FUW Trends in Science & Technology Journal 1 (2) (2016) 456–465.
[30] S. Bae, S. Kim, S. Lee, W. Choi, Dye decolorization test for the activity assessment of visible light photocatalysts, Cataylsts Today 224 (2014) 21–28.
[31] A. Kumar, S. Kumar, A. Bahuguna, A. Kumar, V. Sharma, V. Krishnan, Recyclable, bifunctional composites of perovskite type N-$CaTiO_3$ and rGO as an efficient adsorptive photocatalyst for environmental remediation, Mater. Chem. Front. 1 (11) (2017) 2391–2404.
[32] S.B. Hammouda, F. Zhao, Z. Safaei, V. Srivastava, D.L. Ramasamy, S. Iftekhar, S. kalliola, M. Sillanpaa, Degradation and mineralization of phenol in aqueous medium by heterogeneous monopersulfate activation on nanostructured cobalt based-perovskite catalysts $ACoO_3$ (A=La, Ba, Sr and Ce): characterization, kinetics and mechanism study, Appl. Catal. B Environ. 215 (2018) 60–73.
[33] B. Abebe, H.C.A. Murthy, E. Amare, Summary on adsorption and photocatalysis for pollutant remediation, J. Encapsulation Adsorpt. Sci. 8 (2018) 225–255.
[34] U.A. Edet, A.O. andIfelebuegu, Kinetics, isotherms and thermodynamic modelling of the adsorption of phosphates from model wastewater using recycled brick waste, Processes 8 (665) (2020) 1–15.
[35] F.T. Ademiluyi, J.C. Nze, Sorption characteristics for multiple adsorptions of heavy metal ions using activated carbon from Nigerian *bamboo*, J. Mater. Sci. Chem. Eng. 4 (2016) 39–48.
[36] S.D. Patil, S. Renukdas, N. Patel, Comparative study of kinetics of adsorption of methylene blue from aqueous solutions using cinnamon plant (*Cinnamonum zeylanicum*) leaf powder and pineapple (*Ananas comosus*) peel powder, The Electronic Journal of Chemistry 4 (2) (2012) 77–100.
[37] P. Kajitvichyanukul, J. Ananpattarachai, Adsorption from: Managing Global Resources and Universal Processes, CRC Press, England, 2020, pp. 387–415.
[38] S. Safari, S.M.S. Ahmadian, A.R. Amani-Ghadim, Visible light photocatalytic activity enhancing of $MTiO_3$ perovskites by M-cation (M = Co, Cu and Ni) substitution and gadolinium doping, J. Photochem. Photobiol. Chem. 394 (2020) 112461.
[39] A.L. Mantwa, G.T. Kamohelo, J.M. Selepe, A. Iorkyaa, M.N. Odireleng, Study on Photoluminescence and Energy Transfer of Eu^{3+}/Sm^{3+} Single-Doped and Co-doped BaB_8O_{13} Phosphors, Physica B: Physics of Condensed Matter, 2017.
[40] J.R. Quinones-Gurrola, J.C. Rendon-Angeles, Z. Matamoros-Veloza, J.L. Rodriguez-Galicia, K. Yanagisawa, Rapid one-step preparation of $SrZrO_3$ using Zr^{4+} gel and $SrSO_4$ ore under alkaline hydrothermal conditions, Boletin de La Socidad Espanola de Ceramic Y Vidrio 62 (2022) 479–492.
[41] G.L. Lucena, L.C. de Lima, M.C. Honorio, A.L.M. de Oliveira, R.L. Transqiilim, E. Longo, A.G. de Souza, A.S. da Maia, I.M.G. dos Santos, $CaSnO_3$ obtained by modified Pechini method applied in the photocatalytic degradation of an azo dye, Ceramica 63 (2017) 536–554.
[42] L.A. Alfonso-Herrera, A.M. Huerta-Flores, L.M. Torrez-Matinez, J.M. Rivera-Villannueva, D.J. Ramirez-Herrera, Hybrid $SrZrO_3$-MOF heterostructure: surface assembly and photocatalytic performance for H_2 evolution and degradation of indigo carmine dye, Springer, J. Mater. Sci. Mater. Electron. 29 (2018) 10395–10410.
[43] S. Katyayan, S. Agrawal, Investigation of spectral properties of Eu^{3+} and Tb^{3+} doped $SrZrO_3$ orthorhombic perovskite for optical and sensing applications, J. Mater. Sci. Mater. Electron. 28 (24) (2017) 18442–18454.
[44] J. Huang, L. Zhou, Z. Wang, Y. Lan, Z. Tong, F. Gong, J. Sun, L. Li, Photoluminescence properties of SrZrO3:Eu^{3+} and BaZrO3:Eu^{3+} phosphors with perovskite structure, J. Alloys Compd. 487 (2009) 5–7.
[45] M. Tarrida, H. Larguem, M. Madon, Structural investigations of $(Ca,Sr)ZrO_3$ and $Ca(Sn,Zr)O_3$ perovskite compounds, Phyysics and Chemistry of Minerals 36 (2009) 403–413.
[46] P.R. Jubu, F.K. Yam, K.M. Chahrour, Structural and morphological properties of β-Ga_2O_3 nanostructures synthesized at various deposition temperatures, Phys. E Low-dimens. Syst. Nanostruct. 123 (2020) 1–8.

[47] R.V. Leeuwen, First-principles approach to the electron-phonon interaction, Physical Rewiews, B 69 (2004) 115110.
[48] K.Y. Foo, B.H. Hameed, Insights into the modeling of adsorption isotherm systems, Chem. Eng. J. 156 (1) (2010) 2–10.
[49] S. Ouni, S. Nouri, J. Rohlicek, R.B. Hassen, Structural and electrical properties of the sol-gel prepared $Sr_{1-x}Er_xSnO_{3-\delta}$ compounds, J. Solid State Chem. 192 (2012) 132–138.
[50] D. Triyona, U. Hanifaha, H. Laysandra, Structural and optical properties of Mg-substituted $LaFeO_3$ nanoparticles prepared by a sol-gel method, Results Phys. 16 (2020) 102995.
[51] R.W. Utami, R.A. Rafsanjani, D. Triyono, Optical properties of $La_{0.9}Sr_{0.1}Fe_{1-x}Mo_xO_3$ (x = 0.1, 0.2, and 0.3) perovskite material prepared by sol-gel method, J. Phys. 1153 (2019) 012072.
[52] K. Pan, C. Yang, J. Hu, W. Yang, B. Liu, J. Yang, S. Liang, K. Xiao, H. Hou, Oxygen vacancy mediated surface charge redistribution of Cu-substituted $LaFeO_3$ for degradation of bisphenol A by efficient decomposition of H_2O_2, J. Hazard Mater. 389 (2020) 12207.
[53] V. Perumal, A. Sabarinathan, R. Robert, K.M. Prabu, R. Uthirakumar, Facile synthesis of cationic surfactant-treated hierarchical nanorods SnO_2@CdO nanocomposite photocatalyst for degradation of methylene blue under sunlight, Mater. Today 234 (2012) 223–331.
[54] P.R. Jubu, O.S. Obaseki, F.K. Yam, S.M. Stephen, A.A. Avaa, A.A. McAsule, Y. Yusof, D.A. Otor, Influence of the secondary absorption and the vertical axis scale of the tauc's plot on optical bandgap energy, J. Opt. 51 (3) (2022) 1–10.
[55] G. Cabello, L. Lillo, C. Caro, G.E. Buono-Core, B. Chornik, M. Flores, C. Carrasco, C.A. Rodriguez, Photochemical Synthesis of $AZrO_{3-X}$ thin films (A=Ba, Ca and Sr) and their Characterization, Ceram. Int. 40 (2014) 7761–7768.
[56] M. Anas, A. Ali, A.G. Khan, A. Alhodaib, A. Zaman, T. Ahmad, V. Tirth, A. Algahtani, S. Ahmad, B.S. Abdullaeva, T. Al-Mughanam, M. Aslam, Influence of zirconium (Zr^{4+}) substitution on the crystal structure and optical and dielectric properties of $Sr_{0.8}Mg_{0.2}(Sn_{1-x}\ Zr_x)O_3$ ceramics, ACS Omega 8 (2023) 33794–33801.
[57] P.R. Jubu, T.T. Bem, U.I. Ndeze, E. Danladi, P.I. Kyesmen, V. Mbah, S. Benourdja, D.D. Hile, A.B. Atsuwe, F.K. Yam, Optical and optoelectronic properties of gallium oxide films fabricated by the chemical vapour deposition method, Phys. B Condens. Matter 678 (2024) 1–12.
[58] T. Alammar, I. Hamm, M. Wark, A.-V. Mudring, Low-temperature route to metaltitanate perovskite nanoparticles for photocatalytic applications, Appl. Catal., B 178 (2015) 20–28.
[59] J.B. Bellam, M.A. Ruiz-Preciado, M. Edely, J. Szade, A. Jouanneaux, A.H. Kassiba, Visible-light Photocatalytic Activity of Nitrogen-doped $NiTiO_3$ thin films prepared by a co-sputtering process, RSC Adv. 5 (2015) 10551–10559.
[60] Y. Soltanabadi, M. Jourshabani, Z. Shariatinia, Synthesis of novel CuO/$LaFeO_3$ nanocomposite photocatalysts with superior Fenton-like and visible-light photocatalytic activities for degradation of aqueous organic contaminants, Sep. Purif. Technol. 202 (2018) 227–241.
[61] C.W. Chang, C.C. Hu, Graphene oxide-derived carbon-doped $SrTiO_3$ for highly efficient photocatalytic degradation of organic pollutants under visible light irradiation, Chem. Eng. J. 383 (2020) 123116.
[62] B. Rani, G. Thamizharasan, A.K. Nayak, N.K. Sahu, in: Fosso-Kankeu Elvis, P. Sadanand, S.H. Supraskas (Eds.), Photocatalysts in Advanced Oxidation Processes for Wastewater Treatment, Scriener Publishing Wiley, 2020, pp. 197–257.
[63] P.K. Boruah, P. Borthakur, G. Darabdhara, C.K. Kamaja, I. Karbhal, M.V. Shelke, M.R. Das, Sunlight assisted degradation of dye molecules and reduction of toxic Cr^{+6} in Aqueous Medium using Magnetically recoverable Fe_3O_4/reduced graphene oxide Nanocomposite, RSC Adv. 6 (13) (2016) 11049–11063.
[64] P.O. Oladoye, T.O. Ajiboye, E.O. Omotola, O.J. Oyewola, Methylene blue dye: toxicity and potential elimination technology from wastewater, Results in Engineering 16 (2022) 100678.
[65] T.T.T. Nguyen, T.N. Nguyen, Q.V. Tran, H.K. Nguyen, M.T. Nguyen, T.H.N. Le, Synthesis, Characterization and Effect of pH on degradation of dyes of Cu-doped TiO_2, J. Exp. Nanosci. 11 (2016) 226–238223.
[66] M. Yazdanbakhsh, H. Tavakkoli, S.M. Hosseini, Characterization and evaluation catalytic efficiency of $La_{0.5}Ca_{0.5}NiO_3$nanopowders in removal of reactive blue 5 from aqueous solution, Desalination 281 (2011) 88–395.
[67] H.R. Rajabi, M. Farsi, Effect of transition metal ion doping on the photocatalytic activity of ZnS quantum dots: synthesis, Characterization, and Application for Dye Decolorization, J. Mol. Catal. Chem. 399 (2015) 53–61.
[68] M. Mesbah, S. Hamedshahrakib, S. Ahmadic, M. Sharific, C.A. Igwegbe, Hydrothermal synthesis of $LaFeO_3$ nanoparticles adsorbent: characterization and application of error functions for adsorption of fluoride, MethodsX 7 (2020) 100786.
[69] N. Ayawei, N.A. Ebelegi, D. Wankasi, Modelling and interpretation of adsorption isotherms, Hindawi Journal of Chemistry 2017 (2017).
[70] C.H. Chiou, C.Y. Wu, R.S. Juang, Influence of operating parameters on photocatalytic degradation of phenol in UV/TiO_2 process, Chem. Eng. J. 139 (2008) 322–329.
[71] D. Saha, M.M. Desipio, T.J. Hoinkis, E.J. Smeltz, R. Thorpe, D.K. Hensley, S.G. Fischer-Drowos, J. Chen, Influence of H_2O_2 in enhancing photocatalytic activity of carbon nitride under visible light: an insight into reaction intermediates, J. Environ. Chem. Eng. 6 (4) (2018) 4927–4936.
[72] O. Adedokun, O.S. Obaseki, F.K. Yam, M.D.J. Ooi, O.M. Adedokun, P.R. Jubu, Influence of growth temperature on structural, optical, morphological and photoelectrochemical characteristics of vertically aligned hydrothermally synthesized TiO_2 nanorods, Physica B 688 (2024) 1–9.
[73] C.M. Miller, R.L. Valentine, Mechanism studies of surface catalyzed H_2O_2 decomposition and contaminant degradation in the presence of sand, Water Res. 33 (12) (1999) 2805–2816.
[74] A. Trocha, O. Impert, A. Katafias, R. Van-Eldik, Mechanistic details of the catalytic degradation of MB by H_2O_2 in basic solution, Polyhedron 210 (2021) 115507.
[75] A. Haruna, I. Abdulkadir, S.O. Idris, Photocatalytic activity and doping effects of $BiFeO_3$ nanoparticles in model organic dyes, Heliyon 6 (2020) e03237.